Article:
Xia, D, Li, H, Mannering, J et al. (2020) Electrically Heatable Graphene Aerogels as Nanoparticle Supports in Adsorptive Desulfurization and High-Pressure CO2 Capture. Advanced Functional Materials, 30 (40). 2002788. ISSN: 1616-301X

https://doi.org/10.1002/adfm.202002788

Electrically-Heatable Graphene Aerogels as Nanoparticle Supports in Adsorptive Desulfurisation and High-Pressure CO_2 Capture

Dong Xia, Heng Li, Jamie Mannering, Peng Huang, Xiarong Zheng, Alexander Kulak, Daniel Baker, Diana Iruretagoyena, Robert Menzel**

D. Xia, J. Mannering, Dr. A. Kulak, Dr. R. Menzel
School of Chemistry, University of Leeds, LS2 9JT, Leeds, UK
E-mail: r.menzel@leeds.ac.uk

Dr. D. Iruretagoyena
Department of Chemical Engineering, Imperial College, London SW7 2AZ, UK
E-mail: d.iruretagoyena09@imperial.ac.uk

Dr. H. Li
Key Laboratory of Estuarine Ecological Security and Environmental Health, Tan Kah Kee College, Xiamen University, 363105, Zhangzhou, China

Dr. P. Huang
School of Engineering and Physical Sciences, Heriot-Watt University, EH14 4AS, Edinburgh, UK

X. Zheng
Department of Chemical and Biochemical Engineering, College of Chemistry and Chemical Engineering, and The Key Laboratory for Synthetic Biotechnology of Xiamen City, Xiamen University, 361005, Xiamen, People's Republic of China

Dr. D. Baker
School of Physics and Astronomy, University of Leeds, LS2 9JT, Leeds, UK

Keywords: graphene aerogels, mixed metal oxides, pre-combustion CO_2 capture, desulfurization, Joule heating

Abstract: Hydrotalcite-derived nanoparticles (MgAl-mixed-metal-oxide, NiAl-metal-nanoparticles, CuAl-metal-nanoparticles) were supported on reduced graphene oxide (rGO) aerogels at very high nanoparticle loadings (~ 80 wt%). The presence of the macroporous, 3D-structured rGO aerogel support provides remarkable performance enhancements across a broad range of important functional nanoparticle characteristics due to markedly improved nanoparticle stabilisation and accessibility. Adsorptive desulfurisation experiments show that

supporting MgAl-mixed-metal-oxides (MgAl-MMO) onto rGO aerogels induces substantially increased uptake capacity (>100 % increase), sorption kinetics (>30-fold), and nanoparticle regeneration stability (>3 times) compared to unsupported nanoparticle powders. Importantly, the electrical conductivity of the rGO aerogel network adds completely new functionality by enabling accurate and stable nanoparticle temperature control via direct electrical heating of the graphitic support. Support-mediated resistive heating allows for thermal nanoparticle recycling at much faster heating rates (>700 °C·min^{-1}) and substantially reduced energy consumption, compared to conventional, external heating. For the first time, the CO_2 adsorption performance of MgAl-MMO/rGO hybrid aerogels is assessed under elevated-temperature and high-CO_2-pressure conditions relevant for pre-combustion carbon capture and hydrogen generation technologies. The total CO_2 capacity of the aerogel-supported MgAl-MMO nanoparticles was more than double that of the unsupported nanoparticles, and reached 2.36 mmol·CO_2/g ads (at p_{CO2}=8 bar, T=300 °C), outperforming other high-pressure CO_2 adsorbents.

1. Introduction

Graphene aerogels are sponge-like macroscopic materials constructed from three-dimensional, gas-filled graphene networks, providing an exciting new class of porous materials with great technological promise. The unique characteristics of graphene aerogels are based on the potential for integrating the extraordinary nanoscale properties of exfoliated graphenes with the tuneable, macroscale features of aerogel materials,[1] including tailored porosity,[2] large surface areas,[3] flexible mechanical properties[4] and ultralow density.[5] Consequently, graphene-based aerogels have found first applications in a range of technologies, including environmental remediation,[6] structural composites,[7] biomaterials,[8] electronics,[9] sensors[10]

and energy storage.[11] Integrating inorganic nanoparticles (metal-oxides,[12] metallic nanoparticles,[13] clays,[14] other 2D materials[15] etc.) into graphene aerogels has proven an extremely successful strategy to substantially boost the aerogels' performance in established technologies (e.g. energy storage, sensors)[16] as well as to open up completely new application routes (e.g. in heterogeneous catalysis or piezoelectronics).[14, 17]

For the fabrication of inorganic/graphene hybrid aerogels, wet-chemical nanoparticle assembly approaches have proven particularly popular due to their intrinsic capability for straightforward tuning of crucial macroscopic material characteristics (surface area, porosity, crosslinking density etc.)[18] and intrinsic compatibility with solution-based inorganic nanoparticle synthesis.[16a] Wet-chemical graphene aerogel fabrication typically utilizes graphene oxide (GO), a highly-oxidized, water-processible graphene derivative, that enables 3D network assembly in aqueous solution, typically via hydrothermal or polymer-assisted approaches.[1b] Subsequent lyophilisation and reduction treatments are employed to produce the final reduced graphene oxide (rGO) aerogels with (partially) restored graphitic properties.[8, 19] To embed inorganic nanoparticles within the 3D network of rGO aerogels, a variety of solution-based synthetic approaches has been explored, including aerogel infiltration with pre-formed nanoparticles, aerogel impregnation with inorganic precursor salts, and in-situ nanoparticle formation during hydrothermal aerogel synthesis.[20] The resulting nanoparticle/rGO hybrid aerogels have shown enhanced functional activity and stability in catalytic, sensing and structural applications, mainly based on the support function of the high-surface-area rGO aerogel network. Examples include Pt/rGO aerogels with excellent electro-catalytic performance in the oxygen reduction reaction,[21] Fe_3O_4/rGO aerogels for ultralight, magnetic actuators,[22] MXene/rGO aerogels for fast and highly-sensitive piezoresistive sensors,[23] and complex hybrid Pt/C_3N_4/rGO aerogel catalysts for efficient methanol oxidation.[24]

Recently, graphene-based aerogels have also been successfully hybridised with hydrotalcite-like compounds for applications in solar-driven photo-electrochemical water oxidation (NiFe-LDH/GO aerogels),[25] sodium-ion batteries (NiCo-LDH/GO aerogels)[26] and water treatment (MgAl-LDH/GO aerogels).[27] Hydrotalcite-like compounds, also known as layered double hydroxides (LDH), are lamellar anionic clays that contain (most commonly) a binary mixture of divalent metal ions (e.g. Mg^{2+}, Ni^{2+}, Zn^{2+}, Co^{2+}) and trivalent metal ions (e.g. Al^{3+}, Fe^{3+}) within the clay layers.[27] Due to their flexible chemical composition and excellent atomic metal dispersion, LDH particles provide ideal precursors for other classes of functional inorganic nanoparticles. Mixed metal oxide (MMO) nanoparticles can be easily synthesised through straightforward, scalable calcination or annealing treatments of the LDH parent materials.[28] Under highly-reductive, thermal annealing conditions, nobler metal ions in the LDH precursor materials can also be fully reduced to their metallic state, leading to the formation of metal nanoparticles.

In this study, MMO/rGO aerogels are studied, for the first time, for adsorptive desulfurisation and high-pressure CO_2 capture in order to assess the multifunctional benefits of 3D-structured, electrically-conducting rGO aerogel supports in two technologically-important sorption applications. Unsupported LDH-derived MMO materials have been widely studied for the adsorptive removal of inorganic and organic pollutants from liquids and gases. For example, LDH-derived MMO have shown promise for the adsorptive desulfurisation of fuels, often studied via adsorption of model organosulfur compounds (such as dibenzothiophene, DBT) from hydrocarbon solutions. In terms of organosulfur sorption capacity, LDH-derived MMO nanoparticle systems show only moderate activity (around 1 mg·S/g ads for MgAl-MMO) compared to other porous sorbents (activated carbons, MOFs, zeolites etc.).[29] However, they outperform other solid sorbent systems in a number of other practically-important sorption characteristics, making them overall viable, selective and regenerable sorbents for

desulfurisation applications.[30] The additional benefits of MMO-based sorbents include, non-reactive organosulfur binding (enabling sorbent regeneration via relatively mild temperature- or pressure-swing), good thermal and chemical stability, very good performance in the presence of common, competing adsorbate species (e.g. water), and high selectivity for challenging, sterically-hindered organosulfurs.[28, 31]

In the context of gas-phase sorption applications, the adsorption of CO_2 onto porous solid sorbents is of major technological and environmental importance. LDH-derived MMO materials are particularly interesting sorbents for pre-combustion CO_2 capture and hydrogen generation via sorption-enhanced reaction (SER) processes. SER are based on the in-situ adsorption of CO_2 during conventional hydrogen production reactions (such as water gas shift or steam reforming of methane) to increase the hydrogen yield and, simultaneously, remove CO_2 from the hydrogen product streams. Hydrotalcite-derived MMO nanoparticles are particularly promising chemisorbents for SER technologies as they show their highest CO_2 sorption performance at the relevant high operating temperatures (200-500 °C) and high CO_2 pressures (1-30 bar), typically employed in practical SER processes. Under elevated-temperature conditions, CO_2 physisorbents (e.g. zeolites and activated carbons) have relatively low capacities and selectivities, while other CO_2 chemisorbents (e.g. lithium zirconates and calcium oxides) exhibit slow adsorption kinetics or require high energy to be regenerated.[32]

Despite the positive sorption characteristics of LDH-derived MMO materials for desulfurisation and SER, their overall multicycle performance in terms of capacity, kinetics and stability needs to be further improved before they can be successfully used commercially. The sorption performance of MMO nanoparticles can be significantly limited by particle sintering when they are exposed to successive adsorption and desorption cycles, resulting in significantly reduced soprtion capacities and loss of accessible sorption sites over time. In

addition, the energy efficiency of these sorption systems needs to be further improved so they can be environmentally and economically feasible compared to more mature technologies.[33]

It has been reported that significant performance enhancements of LDH-derived MMOs in both organosulfur and CO_2 sorption can be obtained by dispersing them on high surface area materials, such as carbons.[28, 33b, 34] It has also been shown that graphene-based *powders* provide particularly suitable supports due to matching morphology and surface charge between LDH and GO support.[28, 34] However, there are no studies assessing the benefits of 3D-structured macroscopic graphene supports, such as rGO aerogels, on the MMO performance in these important sorption applications. In addition, the electrical conductivity of rGO aerogels provides a unique opportunity for direct electrical heating of the supported sorbents, with great potential to substantially improve energy efficiency of thermally-driven MMO processes and applications. While electrical heating has been demonstrated for pure rGO aerogels and boron-nitride/carbon-nanotube aerogels,[19b, 35] this valuable additional functionality of the rGO aerogels (not available through other supports, such as nanocarbon powders, zeolites, MOFs) has not yet been explored for the technologically-important MMO nanoparticle systems. Finally, there is also a substantial lack of sorption data for carbon-supported MMO materials under realistic commercial SER operating sorption conditions. While some CO_2 sorption studies have been carried out at the relevant high temperatures (T= 200-500 °C),[36] to the authors' knowledge, there are no studies investigating the sorption characteristics of carbon-supported MMO sorbents at high CO_2 pressures (p_{CO2} > 1 bar).

This study addresses these research gaps by investigating rGO aerogels as stabilising and electrically-responsive supports for LDH-derived nanoparticles to create multifunctional porous materials that combine substantially enhanced performance (across different sorption applications) with the novel capability for energy-efficient, resistive sorbent heating. These principles are investigated by decorating rGO aerogels with very high loading fractions of

LDH-derived mixed metal sorbent nanoparticles (MgAl-MMO, CuAl-MNP, NiAl-MNP). The chemical and structural properties of the resulting hybrid aerogel sorbents are carefully assessed and linked to their fundamental sorption characteristics (capacity enhancement, sorption kinetics, regeneration stability, selectivity), as assessed via liquid-phase organosulfur sorption measurements. The additional functionality of the hybrid aerogels sorbents is demonstrated by exploiting electrical heating of the rGO aerogel framework for rapid thermal MMO sorbent recycling via energy-efficient Joule heating (a practically important process enabled by the hybrid aerogel form, and not possible for MMO sorbents in powder form). To demonstrate the benefits of rGO aerogel support for gas-phase sorption applications, a typical MgAl-MMO/rGO hybrid aerogel sorbent is also investigated for CO_2 sorption under high-pressure (p_{CO2}= 1-10 bar), high-temperature (T= 300 °C) conditions relevant to SER processes, and its performance data assessed against an equivalent unsupported MMO-powder sorbent and literature data on other high-pressure, high-temperature CO_2 sorbents.

2. Results and Discussion

2.1. Hybrid aerogel synthesis

In order to support MMO sorbent nanoparticles within the framework of rGO aerogels at high loadings, hybrid aerogels were produced via polymer-assisted, wet-chemical assembly of LDH-decorated GO. This approach was chosen to avoid potential diffusion-related issues associated with more conventional aerogel decoration methods (i.e. impregnation of pre-assembled aerogel monoliths), and to ensure uniform and high particle loading throughout the entire aerogel. Specifically, hybrid aerogels were synthesised through a facile three-stage fabrication process (**Figure 1**).

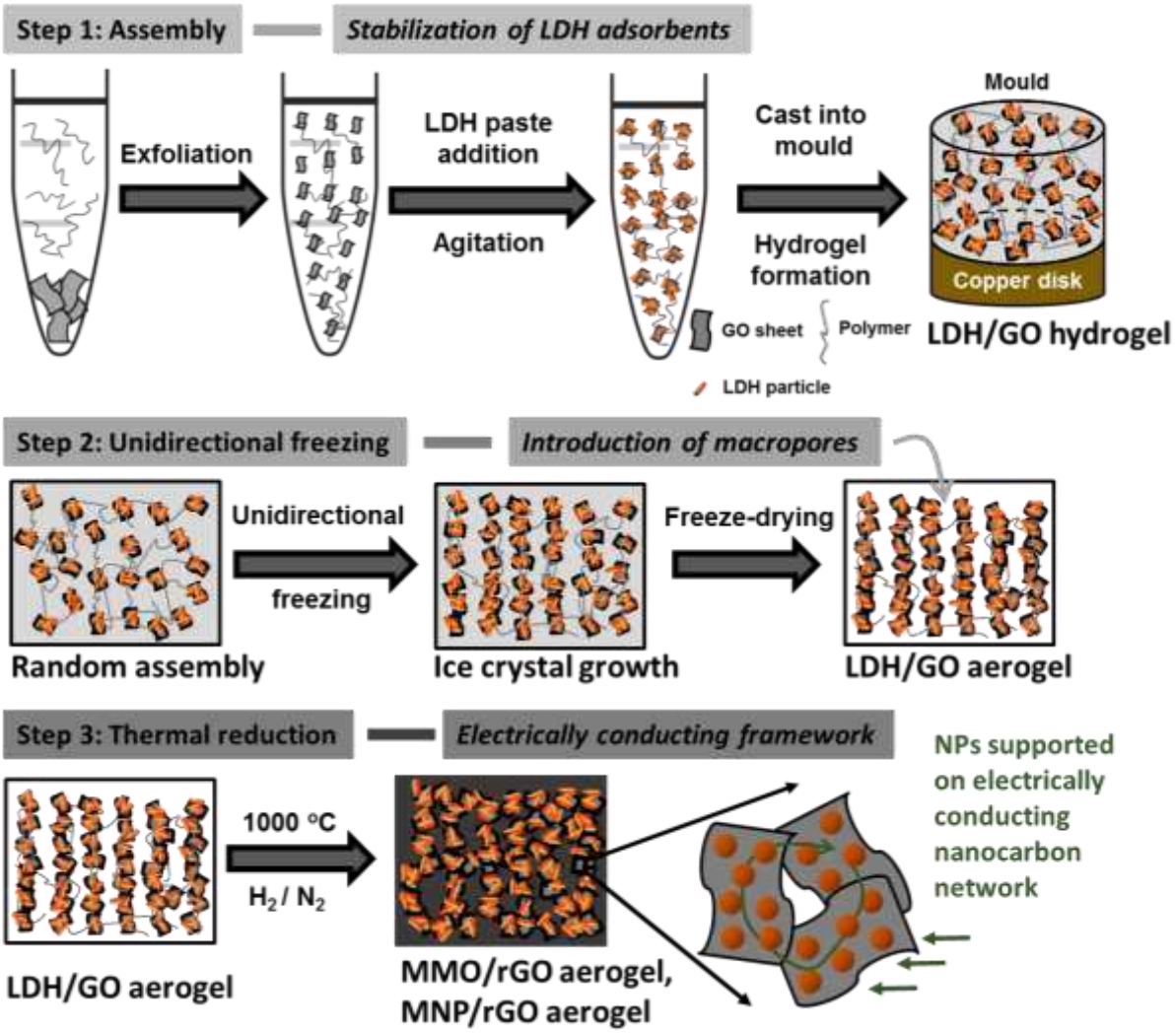

Figure 1. Synthetic procedure for the fabrication of electrically-conducting, high-weight loading sorbent-nanoparticle/rGO hybrid aerogel. MMO = mixed-metal-oxide; MNP = metal nanoparticle.

In Step 1, pre-synthesised LDH particles are thoroughly dispersed within an aqueous GO/polymer dispersion. LDH particles are introduced in form of a wet-paste (rather than a dried powder) in order to aid complete LDH nanoparticle dispersion and individualisation. In this LDH/GO mixture, the positively-charged LDH nanoparticles electrostatically attach to the negatively-charged GO sheets, aiding the formation of LDH-decorated GO sheets in solution. The aqueous mixtures are then cast into cylindrical moulds where, assisted by the polymer additive, the LDH-decorated GO sheets assemble into a stochastic 3D network, resulting in the formation of hydrogels (LDH/GO hydrogel). In Step 2, the LDH/GO hydrogels are frozen, adopting a unidirectional freezing approach (see ESI Figure S1) to induce ice-templated macro-

porosity within the final aerogel monoliths. Subsequent freeze-drying yields cylindrical LDH/GO aerogel monoliths. In Step 3, high-temperature annealing in a reducing atmosphere was employed to produce the final nanoparticle/rGO hybrid aerogel in the form of cylindrical monoliths. The annealing treatment is required to remove the polymer additive from the final products and to promote covalent nanocarbon crosslinking (enhancing the hybrid aerogels' structural stability, important for their practical application as sorbents). The high-temperature treatment also results in the conversion of the supported LDH particle into MMO or metallic nanoparticles (MNP), depending on the chemical composition of the initial LDH particles (see also section 2.2). Crucially, the annealing treatment also restores the graphitic crystallinity of the nanocarbon framework, rendering the final hybrid aerogel sorbents electrically-conducting and, hence, electrically-heatable.

2.2 Hybrid aerogel characterisation

As an important model system, MgAl-MMO/rGO hybrid aerogels were synthesised from MgAl-LDH (atomic Mg:Al ratio 2:1) and GO. Zeta-potential measurements confirm that the initial MgAl-LDH particles and GO sheets carry substantial, opposite surface charge (ζ_{LDH}= +41.8 mV; ζ_{GO}= -31.1 mV, **Figure 2a**). The resulting electrostatic attraction drives efficient and strong particle attachment onto the GO sheets in Step 1 and contributes to the firm anchoring and stabilisation of the functional nanoparticles within the final rGO aerogels.[37] The maximum nanoparticle loading within the rGO aerogels achievable through our synthetic approach was exceptionally high at 78 wt% (as measured by TGA, Figure 2e). Hybrid aerogels with lower nanoparticle loadings can also be easily synthesised (see ESI Figure S2). However, high nanoparticle weight loadings are highly beneficial for sorption applications (as the 'parasitic' weight of the support framework is minimised),[38] and are difficult to achieve by other synthetic strategies (such as aerogel monolith impregnation).[39]

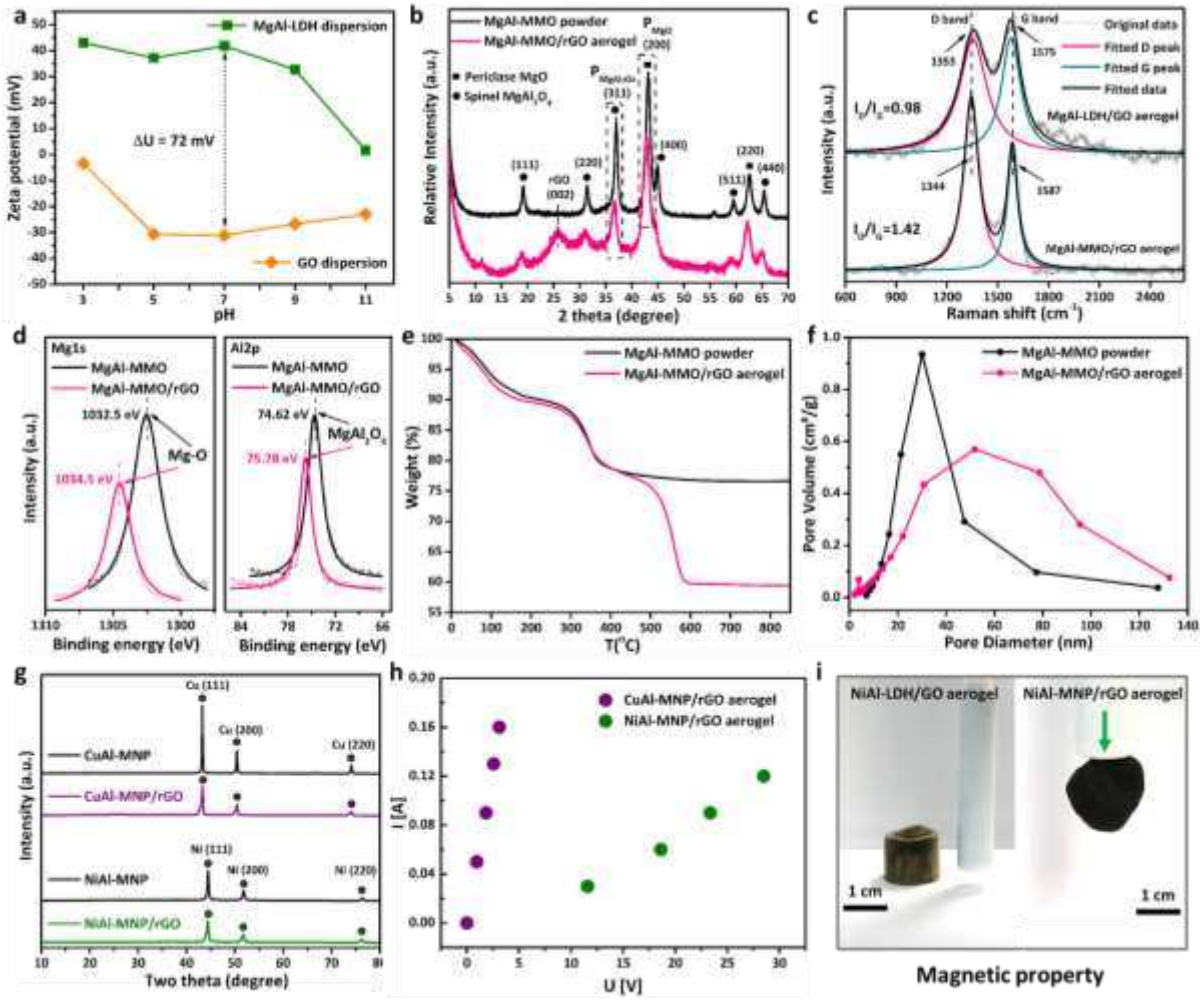

Figure 2. a) Zeta potential of the initial MgAl-LDH and GO suspensions at different pH values. b) XRD of the MgAl-MMO powder and MgAl-MMO/rGO aerogel. c) Raman spectra of initial MgAl-LDH/GO aerogel (product of Step 2) and final MgAl-MMO/rGO aerogel (Product of Step 3). d) High-resolution Mg1s and Al2p XPS spectra of MgAl-MMO powder and MgAl-MMO/rGO aerogel. e) TGA of MgAl-MMO powder and MgAl-MMO/rGO aerogel in air. f) BJH pore-size distribution of MgAl-MMO powder and MgAl-MMO/rGO aerogel. g) XRD of CuAl-MNP powder and NiAl-MNP powder, and the corresponded rGO hybrid aerogels. h) I-V characteristics of the CuAl-MNP/rGO aerogel and the NiAl-MNP/rGO aerogel. i) Digital images of the initial NiAl-LDH/GO aerogel and the final NiAl-MNP/rGO aerogel next to a magnet.

Conversion of MgAl-LDH into MgAl-MMO particles upon thermal annealing in Step 3 is confirmed by XRD (Figure 2b, ESI Figure S3). Specifically, a mixture of MgO and $MgAl_2O_4$ is formed, as evidenced by sets of characteristic periclase (MgO) and spinel ($MgAl_2O_4$) peaks, in line with well-known MgAl-LDH annealing transformations.[40] Scherrer analysis of the XRD peak widths indicates that the aerogel-supported nanoparticles exhibit almost 50 % smaller crystallite domain sizes compared to unsupported nanoparticles (**Table 1**), confirming

that nanoparticle anchoring within the graphitic aerogel is strong and effectively inhibits sintering during annealing. Interestingly, XPS analysis (Figure 2d) also indicates strong interactions between the graphitic aerogel framework and the MMO nanoparticles. While the MgAl-MMO powder exhibits Mg1s and Al2p peaks at 1032.5 eV and 74.6 eV (characteristic for Mg and Al oxides),[41] the MgAl-MMO/rGO aerogels exhibit noticeably shifted Mg1s and Al2p peaks, suggesting charge transfer between the rGO surfaces and the MgAl-MMO particles.

The thermal annealing treatment also successfully re-graphitises GO into an interconnected, electrically conducting rGO framework. The successful formation of rGO is indicated by the characteristic (002) reflection at 26.3° in the XRD pattern of the final hybrid aerogel (Figure 2b). Scherrer analysis suggests that the rGO aerogel support framework consists of few-layer rGO (five rGO sheets per average stack, see ESI Figure S4).[42] Significant increase in the graphiticity of the graphene oxide support framework is confirmed by Raman spectroscopy, as indicated by a marked increase in I_D/I_G ratio from 0.98 to 1.42 (Figure 2c); consistent with Raman studies of thermally-treated GO in the literature.[43] Importantly, re-graphitisation upon thermal treatment results in the restoration of electrical conductivity. Even at very high contents of (electrically-insulating) MgAl-MMO, the hybrid aerogel exhibits excellent electrical conductivity of up to 15 $S \cdot m^{-1}$, thereby opening up routes for framework-mediated electrical stimulation and electrical-heating of the supported nanoparticles. BET measurements (Figure 2f, ESI Figure S5) suggest excellent nanoparticle dispersion on the 3D rGO network and minimised particle aggregation, even at high MMO loadings, as indicated by an almost 100 % larger specific surface area of the aerogel-supported MgAl-MMO particles compared to the unsupported powder. The MgAl-MMO/rGO aerogel also exhibits a considerably broader mesopore distribution (Figure 2f) with a larger mean mesopore size ($d_{mesopore}$ ~ 50 nm),

compared to the unsupported powder adsorbents ($d_{mesopore}$ ~ 30 nm) (Table 1), indicative of a more spaced, less aggregated nanoparticle morphology in the hybrid aerogels.

Table 1. Materials characteristics of MgAl-MMO powder (pure, unsupported MgAl-MMO nanoparticles) and MgAl-MMO/rGO hybrid aerogel (MgAl-MMO nanoparticles supported within rGO aerogels at a weight loading of 78 wt%).

Sorbent	Density (mg/cm^3)	Conductivity (S/m)	MMO size (XRD)[a)] (nm)	MMO size (SEM)[b)] (nm)	SSA (BET) (m^2/g)	Mesopore size[c)] (nm)
MgAl-MMO powder	756.5	0	12.9	131	49.7	30
MgAl-MMO/rGO aerogel	18.3	15	7.4	68	96.8	52

[a)]Crystallite domain sizes, as derived from the (311) $MgAl_2O_4$ XRD peak widths (Figure 2b); [b)]Average size of MMO particles, as measured by SEM (ESI, Figure S6 and S7); [c)]Average mesopore diameters, as derived from the BJH mesopore size distributions (Figure 2f).

SEM imaging confirmed the differences in overall material morphology (**Figure 3**). The SEM of the MgAl-MMO/rGO aerogel showed smaller particles (~70 nm, Figure 3c, ESI Figure S6), evenly distributed across the rGO surface at relatively high density. Uniform MgAl-MMO particle distribution is further confirmed by EDX mapping of an individual hybrid aerogel 'flake', exhibiting uniform Mg distribution across the whole flake (Figure 3g and 3h). Lower magnification SEM showed larger internal pores of around 30 μm diameter (Figure 3b, ESI Figure S6). These macropores are due to ice-crystal growth induced by unidirectional freezing during fabrication and are likely to be beneficial for adsorption application, by aiding adsorbate diffusion to active sorption sites within the aerogel interior. TEM images of the hybrid aerogels show that the MgAl-MMO particles observed in SEM are clusters of smaller primary nanoparticles (10 - 20 nm, similar in size to the crystallite domain sizes observed via XRD) (Figure 3d-3f). TEM also visualises the relatively thin GO sheets, difficult to observe by SEM.

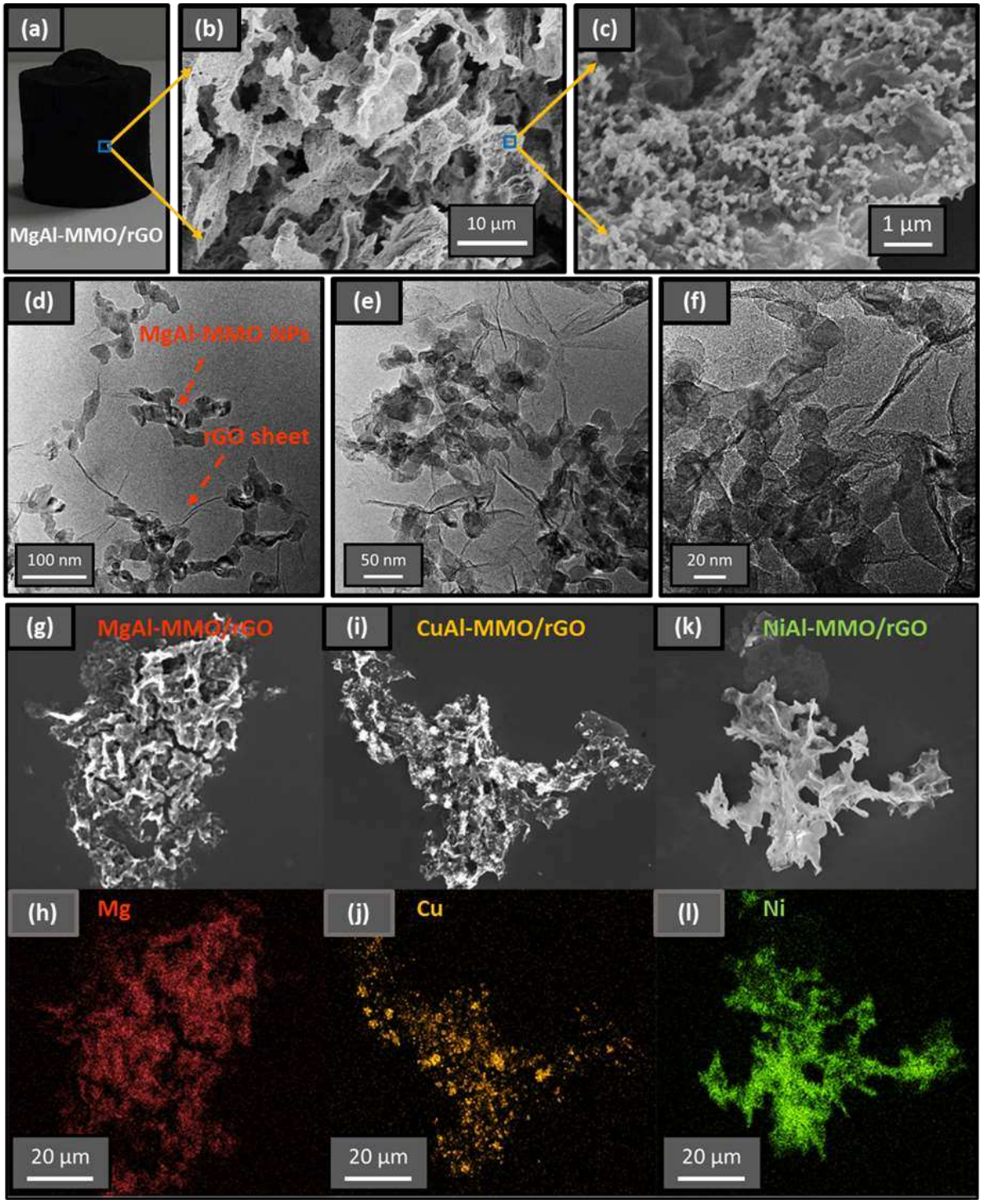

Figure 3. a) Digital image of a MgAl-MMO/rGO aerogel monolith. b) and c) SEM images of MgAl-MMO/rGO aerogel. d) - f) TEM images of the MgAl-MMO/rGO aerogel at different magnifications. SEM images of the MgAl-MMO/rGO aerogel (g), CuAl-MMO/rGO aerogel i), and NiAl-MMO/rGO aerogel k), and EDX mapping of Mg h), Cu j), and Ni l) distributions in the corresponded aerogels.

The synthetic methodology used can be easily adapted to introduce other types of nanoparticles, such as MNP, which have a wide range of applications beyond sorption,

293 including as heterogeneous catalyst systems and supercapacitor electrodes. CuAl-MNP and
294 NiAl-MNP systems were also synthesised from their respective LDH precursor particles.
295 Thermal treatment in Step 3 results in the complete reduction of the LDH precursor particles
296 into copper and nickel metal nanoparticles (as confirmed by XRD, see Figure 2g) under the
297 thermal treatment conditions. (Reduction of the aluminium is unlikely under these conditions
298 and is potentially present as amorphous aluminium oxide.)[44] The metallic Cu and Ni
299 nanoparticles can also be supported at high weight loadings within the rGO aerogels (78 wt%
300 and 88 wt%, ESI Figure S10). Both the CuAl-MNP/rGO and NiAl-MNP/rGO aerogels exhibit
301 excellent electrical conductivity (7.7 S/m and 0.2 S/m, see ESI Table S2) and repeatable I-V
302 characteristics (Figure 2h), highlighting the suitability and stability of the hybrid aerogel
303 systems for electrical heating applications. Interestingly, the NiAl-MNP/rGO aerogels also
304 showed clear magnetic properties (Figure 2i), a unique additional functionality of the Ni-based
305 hybrid aerogel systems, that could be highly beneficial in sorption application (e.g. by enabling
306 simple magnetic recovery of spent aerogel sorbents). SEM images and EDX mapping of hybrid
307 aerogel 'flakes' (Figure 3i-3k) show again a highly uniform distribution for the Cu and Ni
308 particle systems (Figure 3j-3l). These findings demonstrate the general applicability of our
309 synthetic approach to produce a wide range of electrically-conducting (and hence electrically-
310 heatable) aerogel-supported nanoparticle systems for different applications.

311 **2.3. Liquid-phase organosulfur sorption**

312 In a first set of experiments, the MgAl-MMO/rGO hybrid aerogels were assessed via liquid-
313 phase organosulfur sorption experiments, specifically, the adsorption of DBT from n-octane
314 solution (**Figure 4**). DBT sorption provides an excellent model system to assess sorption-
315 related benefits imparted by rGO aerogel supports on inorganic nanoparticles across a broad
316 spectrum of important sorption characteristics, including uptake capacities, sorption kinetics,
317 sorption isotherms, selectivity and sorbent re-cycling (Figure 4, **Table 2**).

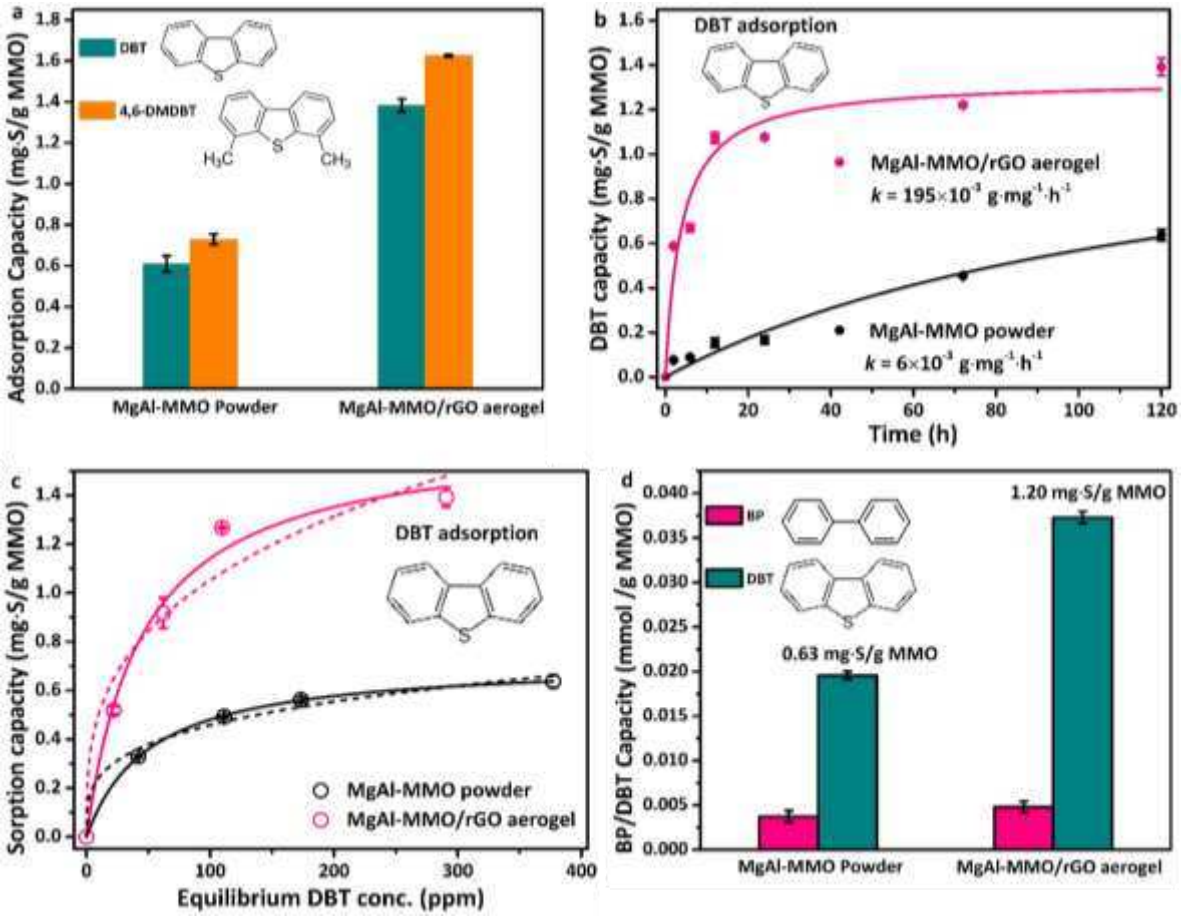

Figure 4. Liquid-phase organosulfur sorption characteristics of MgAl-MMO/rGO aerogels, compared to MgAl-MMO powders: a) Equilibrium uptake capacities for sorption of DBT and DMDBT from n-octane (initial concentration 500 ppm); b) Uptake kinetics for sorption of DBT from n-octane (initial concentration 500 ppm), c) Uptake isotehrms for sorption of DBT from n-octane (initial concentrations tested at 100 ppm, 200 ppm, 300 ppm and 500 ppm, respectively). The dash line is fitted via Freundlich model and the solid line is fitted via Langmuir model; d) Organosulfur selectivity: DBT uptake capacities from n-octane (initial concentration 500 ppm) in the presence of biphenyl (initial concentration 500 ppm).

In terms of equilibrium capacity (at 500 ppm initial organosulfur concentration), the DBT uptake of the aerogel-supported MgAl-MMO was more than double compared to the unsupported nanoparticles (Figure 4a, Table 2), in line with the larger surface area and improved particle dispersion of the hybrid aerogel samples. Similarly, the DBT sorption isotherms (Figure 4c) indicate a doubling of the maximum DBT uptake capacity of the MgAl-MMO/rGO aerogel, compared to that of the unsupported powder (Figure 4c, ESI Table S4). Interestingly, a large increase in equilibrium capacity (123 % increase) is also observed for the uptake of 4,6-dimethyldibenzothiophene (4,6-DMDBT), a sterically hindered organosulfur that

is particularly difficult to remove via conventional desulfurisation processes.[35] It is worth noting that pure rGO aerogels (i.e. rGO aerogels without any nanoparticle loading) exhibited no measureable DBT or DMDBT uptake, i.e. there is no significant organosulfur sorption onto the rGO framework itself. The observed improvements in adsorption performance therefore exclusively stem from improved particle dispersion on the open, high-surface-area nanocarbon framework and the resulting higher concentration of accessible MMO sorption sites. Similar improvements in uptake capacity are observed for the CuAl-MNP/rGO aerogel and NiAl-MNP/rGO aerogels (ESI Table S3). This consistently observed enhancement in sorption capacity clearly confirms the generic benefits of supporting LDH-derived nanoparticles within rGO aerogels in terms of improved sorption-site accessibility and stabilisation against nanoparticle deactivation, relevant to other important applications beyond sorption such as catalysis or energy storage.

Beyond these marked improvements in capacity, the rGO aerogels also induce substantial improvements in other important sorption characteristics, such as kinetics and recycling stability, without diminishing the high organosulfur selectivity of the MgAl-MMO system. In terms of sorption kinetics, the MgAl-MMO/rGO aerogel sorbents show a remarkable acceleration in organosulfur uptake, more than 30 times faster compared to the unsupported powder (as determined from the pseudo-second-order fit of the uptake kinetics, Table 2, Figure 4b). This dramatic acceleration is likely caused by significantly improved diffusion of the organosulfur adsorbates into the MMO/rGO aerogel adsorbents, due to a combination of large, open macroporosity (as observed by SEM) and an increased average mesopore size (as observed by BET), facilitating mass transfer both on the macro- and micro-scale.

In terms of practically very important organosulfur selectivity, competitive adsorption experiments, using DBT/biphenyl mixtures (molar ratio 1:1), show that the presence of sulfur-free aromatics (common hydrocarbon impurities) does not interfere with the efficient and

selective uptake of DBT (Figure 4d, Table 2). In terms of sorbent recycling, the stabilising effect of the rGO framework allows for highly-effective thermal (temperature-swing) regeneration of the MMO nanoparticles. The recycled MgAl-MMO/rGO aerogel sorbents show excellent, high retention of DBT uptake capacity upon thermal regeneration at 250 °C in a Muffle furnace (retention of almost 95 % of the original DBT capacity after three regeneration cycles), in contrast to the poor capacity retention (only 16 %) of the unsupported MgAl-MMO powders (Table 2). In addition, the monolithic shape of the hybrid aerogels also allows for easy recovery of the spent sorbent from solution, another benefit for liquid-phase sorption application due to the avoidance of lengthy or energy-intensive separation methods.

Table 2. Relative enhancements in liquid-sorption characteristics of MgAl-MMO/rGO aerogels (sorbent nanoparticles supported within rGO aerogels, loading fraction 78 wt%) compared to MgAl-MMO powder (unsupported sorbent nanoparticles), as measured via DBT uptake from n-octane solution (500 ppm DBT, 20 °C).

	CAPACITY	**KINETICS**	**SELECTIVITY**	**RECYLABILITY**
Sorbent	DBT equilibrium uptake[a] (mg S/g MMO)	DBT sorption rate constant[b] (10^{-3} g·mg^{-1}·h^{-1})	DBT Selectivity against BP[c] (%)	Capacity retention after 3 regeneration cycles[d] (%)
MgAl-MMO powder	0.64	6	84%	16%
MgAl-MMO/rGO aerogel	1.39	195	87%	95%
RELATIVE ENHANCMENT	**Capacity increase by 117%**	**Kinetics accelerated by a factor of 32**	**Selectivity remains high**	**Regeneration stability improved by a factor of 6**

[(a)] DBT uptake from n-octane after 120 h (see Figure 4a); [(b)] rate constant of adsorption kinetics fitted to pseudo-second-order model (see Figure 4b); [(c)] as determined from competitive sorption of DBT/BP mixtures from n-octane (see Figure 4d; selectivity = molar DBT uptake relative to combined molar uptake of DBT and BP); [(d)] as determined from repeated sorbent re-use after thermal regeneration at 250 °C in a Muffle furnace (see ESI, Figure S18, capacity retention = DBT uptake after 3 regeneration cycles relative to initial DBT uptake).

2.4. Thermal sorbent regeneration via electrical framework heating

Apart from its stabilising function, the rGO aerogel supports also provide important additional functionality, including the capability for electrical nanoparticle heating. Electrical heating is enabled by the excellent electrical conductivity of the interconnected 3D rGO support framework (even at high particle loadings) as well as the aerogels' defined monolithic shape and robust mechanical properties (allowing easy contacting with macroscopic electrodes,

Figure 5a and ESI Figure S14). Using a simple electrode setup, a model hybrid aerogel (MgAl-MMO/rGO aerogel) was electrically heated up to 400 °C in N_2 atmosphere (**Figure 5**).

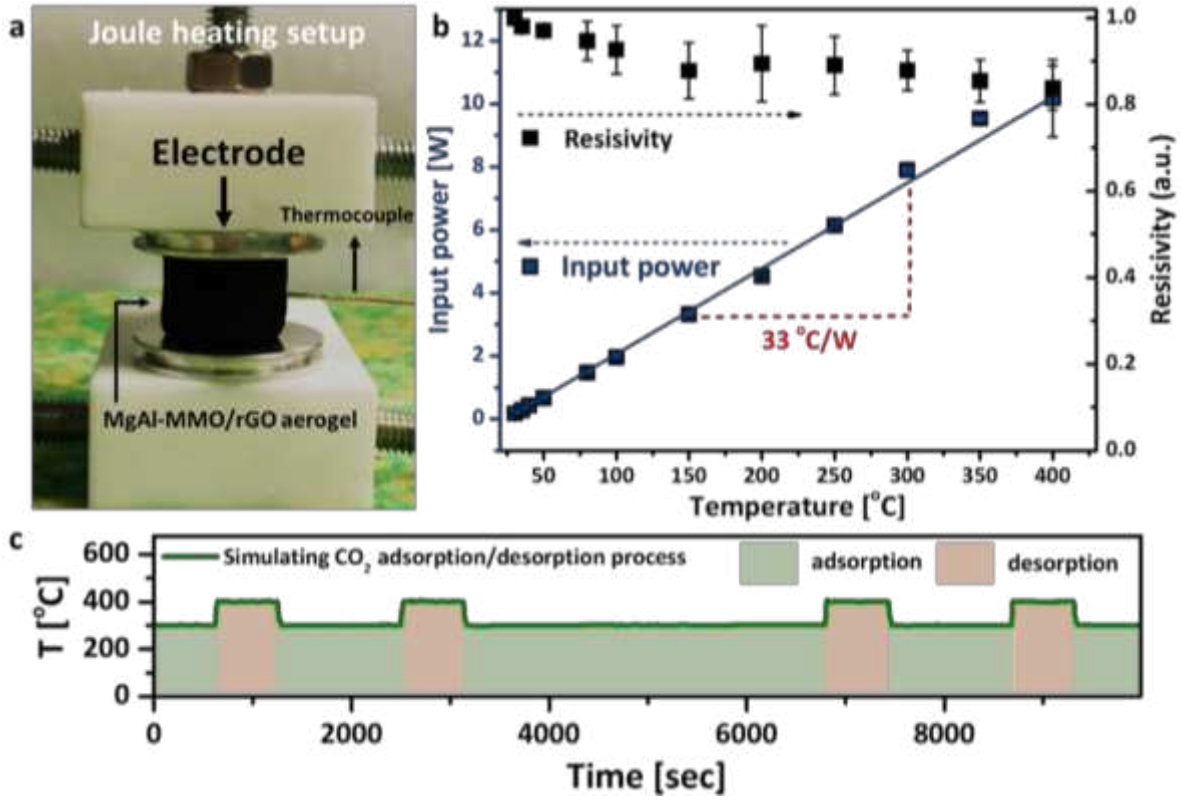

Figure 5. a) Digital image of an MgAl-MMO/rGO aerogel (78 wt% nanoparticle loading) in a Joule heating set-up. b) Relationship between electrical input power and aerogel Joule-heating temperature (measured at the aerogel surface); the right-hand y-axis shows the relative electrical through-volume resistivity of the aerogels at different Joule-heating temperatures. c) Joule-heating temperature stability of MgAl-MMO/rGO aerogel over extended time periods at temperatures relevant to MMO applications in pre-combustion CO_2 capture.

The Joule-heating temperature of the MgAl-MMO/rGO aerogels scales linearly with electrical power input, enabling repeatable and accurate nanoparticle temperature control over a wide temperature range through simple adjustment of power input (Figure 5b). The Joule-heating efficiency for the MgAl-MMO/rGO aerogels, as indicated by the gradual change of temperature with electrical power input, dT/dP, is high at 33 °C/W, which is on the same order of magnitude as observed for the Joule-heating of pure, nanoparticle-free rGO films and aerogels of similar dimensions.[19b, 45] Small, reversible changes in electrical resistivity (reduction by about 20 % at 400 °C) are observed at higher temperatures (Figure 5b) and suggest minor structural changes in the hybrid aerogels upon heating (thermal expansion,

405 desorption of ambient impurities etc.). However, these resistivity changes are fully reversible
406 upon cooling and do not impact on the repeatability of the linear Joule-heating behaviour. Once
407 a set temperature is reached (often within seconds, see also **Figure 6d**), the Joule heating
408 temperature remains extremely stable. To demonstrate this temperature stability, MgAl-
409 MMO/rGO aerogels were electrically-heated to 300 °C and 400 °C (application-relevant
410 temperatures, linked to the thermal activation of CO_2 adsorption and CO_2 desorption on MgAl-
411 MMO, as mentioned in section 2.5) over repeated long periods of up to one hour (Figure 5c).
412 The resulting temperature profile shows that the aerogels can reliably be heated to very stable
413 temperatures, rendering temperature control via framework Joule heating highly feasible for
414 practical applications (ESI Figure S15-S16).

415 In order to demonstrate practical utility, Joule heating was employed to thermally regenerate
416 MgAl-MMO/rGO aerogel sorbents after DBT adsorption. Conventionally, solid organosulfur
417 sorbents are regenerated via washing at elevated temperatures (consuming large volumes of
418 organic solvents) or through external sorbent heating in a furnace (consuming large amounts
419 of energy). Here, Joule heating of the rGO aerogel framework (not possible for unsupported,
420 electrically-insulating metal oxide sorbents) was exploited as an alternative regeneration
421 approach with much lower energy cost.

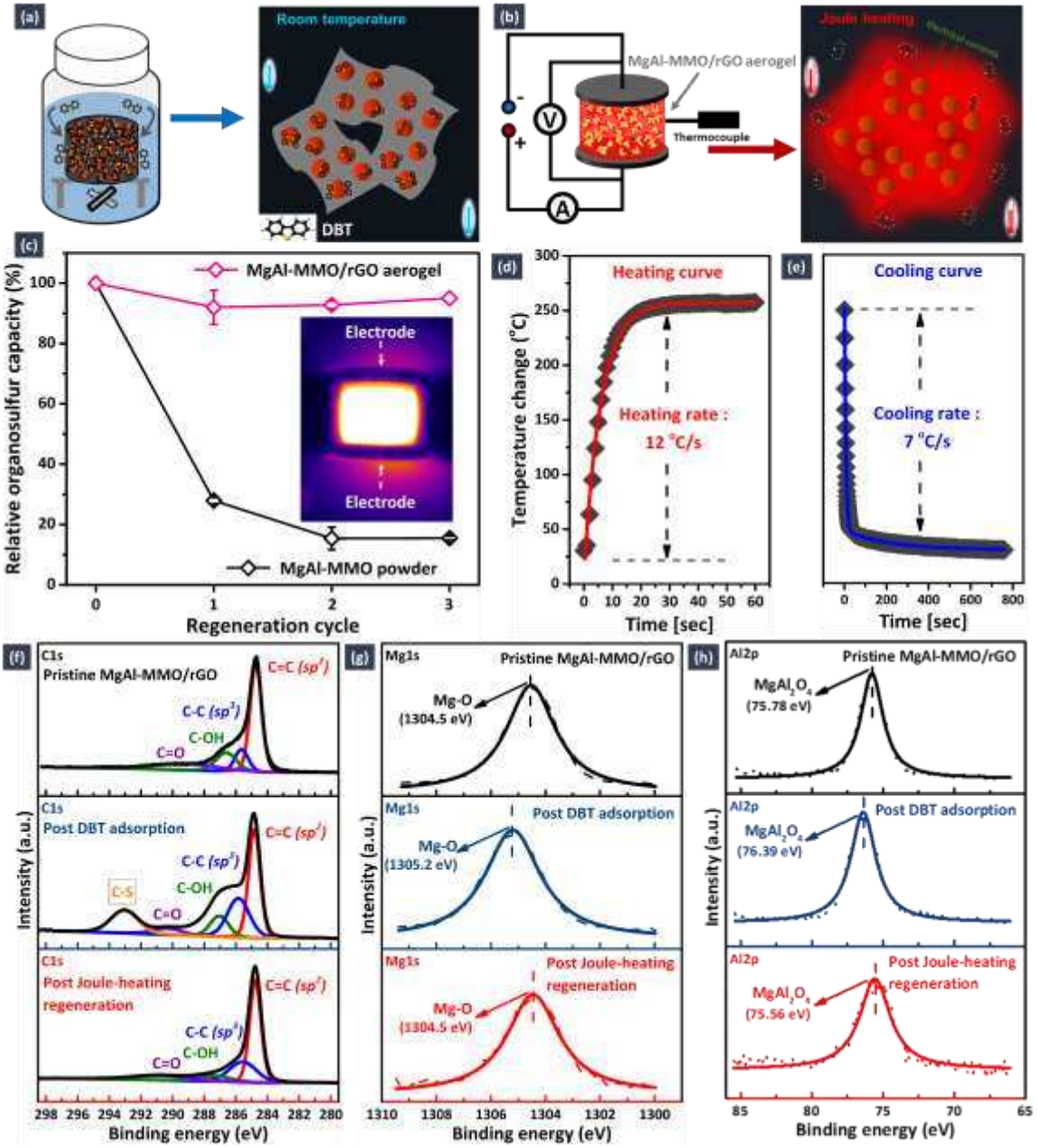

Figure 6. Joule heating regeneration of exhausted MgAl-MMO/rGO hybrid aerogel sorbents. a) Schematic of liquid-phase DBT adsorption onto a hybrid aerogel monolith; b) Schematic of Joule-heating regeneration of a hybrid aerogel sorbent after DBT adsorption. c) Thermal regeneration stability of MgAl-MMO powder (regenerated in a Muffle furnace, black curve), and MgAl-MMO/rGO aerogel (regenerated via Joule-heating, purple curve); insert: thermal image of the Joule-heated MgAl-MMO/rGO aerogel. d) Joule-heating kinetics of MgAl-MMO/rGO aerogel and, e) Natural cooling kinetics of MgAl-MMO/rGO aerogel.(f-h) XPS analysis of the MgAl-MMO/rGO aerogel sorbent in its pristine state (as-synthesized sorbent), post-sorption state (i.e. sorbent after maximum adsorptive DBT uptake from n-octane), and post-regeneration state (i.e. after Joule-heating regeneration of the post-sorption sorbent): f) C1s, g) Mg1s and h) Al2p high-resolution XPS spectra.

Joule heating of post-sorption MgAl-MMO/rGO aerogel sorbents to 250 °C (electrical current input 1 A) resulted in a very successful sorbent regeneration (Figure 6a-6c, purple curve in

Figure 6c). XPS analysis confirms complete removal of the organosulfur adsorbates after Joule-heating as indicated by the disappearance of a characteristic, DBT-related peak in the XPS C1s spectrum (Figure 6f). The regenerated MgAl-MMO/rGO aerogel sorbents can be readily re-used in new adsorptive DBT removal experiments. Importantly, the organosulfur capacity remains very high (around 90 % of the initial capacity) over repeated Joule heating regeneration cycles (Figure 6c), highly beneficial for real-life applications. XPS analysis of the hybrid MgAl-MMO/rGO aerogel before and after regeneration confirms that Joule heating regeneration can be carried out without degradation of the sorbent system. For example, a shift of the Mg1s and Al2p XPS peaks observed after DBT adsorption (likely due to adsorbate-induced charge transfer) is fully reversed upon Joule heating regeneration, suggesting that the MMO particles are restored to their original (pre-sorption) chemical state (Figures 6g and 6h). Similarly, XPS and Raman analysis confirm that Joule heating regeneration does not cause any oxidative damage to the rGO aerogel support framework, as indicated by an unchanged fraction of sp^2 carbon (XPS, Figure 6f and ESI Table S6)[46] and an unchanged I_D/I_G ratio (Raman, ESI Figure S17) before and after regeneration. Importantly, direct electrical heating (~0.9 W·h) also allows for sorbent nanoparticle regeneration at much lower energy cost, compared to conventional, furnace-based regeneration at the same temperature (~ 350 W·h, see also ESI Table S7). The reduction in energy consumption is mainly due to the local nature of the resistive heating process, allowing to directly heat nanoparticles on their support framework, without the need for any wasteful external heating processes. A significant additional factor is that electrical framework heating also enables extremely fast heating of the supported nanoparticles. Through Joule heating, regeneration-relevant temperatures can be reached within seconds (in contrast to relatively slow external heating processes), further reducing the energy costs of the sorbent regeneration process. Specifically, the investigated MgAl-MMO/rGO hybrid aerogels exhibited heating rates of up to 720 $K \cdot min^{-1}$ (reaching 250 °C in

462 less than 20 s). Interestingly, the high thermal conductivity and large porosity of the rGO
463 aerogel supports also gives rise to very fast thermal energy dissipation once electrical heating
464 is switched off (see ESI Figure S16), enabling extremely fast cooling (cooling rates around 420
465 $K \cdot min^{-1}$). The combination of fast heating and cooling kinetics allows for very rapid
466 temperature cycling of the supported nanoparticles which might be exploited for energy-
467 efficient cycling of fast adsorption or catalytic processes in the future. These findings highlight
468 the broad range of advantages of framework-mediated direct, electrical heating of functional
469 nanoparticles compared to conventional thermal approaches, in terms of reduced energy
470 consumption, temperature stability and rapid thermal cycling kinetics.

471 **2.5. High-pressure, elevated-temperature CO_2 adsorption**

472 The rGO aerogel support also gives rise to substantial improvements in functional nanoparticle
473 performance in gas-phase sorption systems. As an important model application, CO_2 sorption
474 at elevated temperatures (T=300 °C) was investigated. Importantly, in this study, elevated-
475 temperature CO_2 sorption was studied at technically-challenging, but practically-important
476 high CO_2 pressure conditions (up to 10 bar total CO_2 pressure, **Figure 7**). In fact, this study
477 presents the first example of investigating inorganic/graphene hybrid aerogels for elevated-
478 temperature CO_2 sorption at high-CO_2-pressures (p_{CO2} > 1 bar) - crucial operating conditions
479 for pre-combustion carbon capture technologies. At these challenging conditions (T= 300 °C,
480 p_{CO2} = 8 bar), the MgAl-MMO/rGO aerogel exhibits an excellent intrinsic CO_2 capacity of 3.02
481 mmol·CO_2/g MMO (Figure 7b, **Table 3**), which corresponds to a high total CO_2 capacity value
482 of 2.36 mmol·CO_2/g ads. Both intrinsic and total CO_2 capacities of the MgAl-MMO/rGO
483 aerogels markedly outperform other solid-state CO_2 sorbents (e.g. activated carbons,
484 commercial MOFs, metal-oxides, zeolites), assessed under comparable elevated-temperature,
485 high-CO_2-pressure conditions (Figure 7d, ESI Table S8, S9, S10).[36]

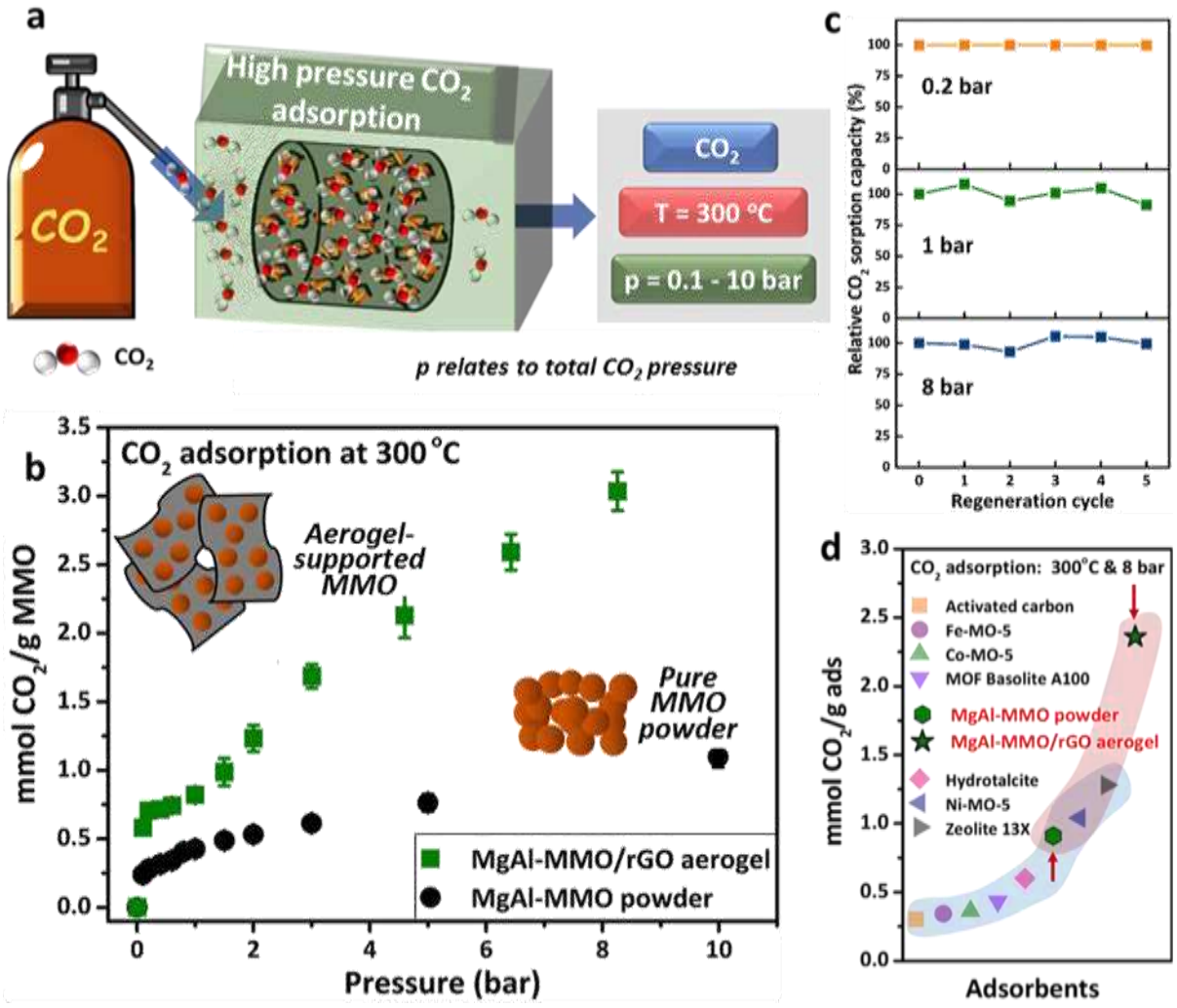

Figure 7. a) Schematic of high-pressure pre-combustion CO_2 adsorption on MgAl-MMO/rGO aerogels. b) high-pressure CO_2 adsorption isotherms onto MgAl-MMO powder and MgAl-MMO/rGO aerogel at 300 °C at total CO_2 pressure of 0.2-10 bar. c) Relative CO_2 capacity retention of the MgAl-MMO/rGO aerogel over five thermal regeneration cycles at 400 °C at 0.2, 1, and 8 bar CO_2 pressure. (d) High-pressure CO_2 sorption capacities (8 bar, 300 °C) of the MgAl-MMO powder and MgAl-MMO/rGO aerogel sorbents prepared in this work, compared against different solid-state sorbent systems, reported in the literature (see also ESI Table S3).

The MgAl-MMO/rGO aerogel shows markedly improved intrinsic CO_2-capacity, compared to the unsupported MMO powder, over a wide CO_2 pressure range (p_{CO2}=0.2-10 bar), as shown in the high-pressure CO_2 sorption isotherm (Figure 7b). This CO_2 capacity enhancement, induced by the rGO aerogel support, is particularly pronounced under high pressure conditions: at 8 bar, the intrinsic CO_2 uptake capacity of the MgAl-MMO/rGO aerogel is over 230 % higher than that of the already well-performing unsupported MgAl-MMO powder (Figure 7b, Table 3). This remarkable enhancement stems to a large extend from the improved nanoparticle

dispersion and excellent MMO accessibility on the aerogel support framework. An important secondary effect is very likely related to the stabilization of the aerogel-supported sorbent against particle compaction at high gas pressures. It is noticeable in Figure 7b, that powder and aerogel isotherms diverge particularly strongly at high CO_2 pressure (>1 bar). Under such high-pressure conditions, loose powder sorbents will experience significant compaction and pore collapse, and, hence, loss of accessible surface area. In contrast, the crosslinked nanocarbon framework in the hybrid aerogel sorbents provides mechanical support against particle compaction, allowing to maintain much better sorption site accessibility at high gas pressures. The unusual isotherm shape of MgAl-MMO/rGO aerogel however suggests that changes in porosity in the hybrid aerogels at gas-pressures >1bar are complex, providing a highly interesting area for future structure-function studies.

Table 3. CO_2 uptake of MgAl-MMO powder and MgAl-MMO/rGO aerogel at different pressures (300 °C working temperature)

CO_2 Pressure	**Intrinsic CO_2 capacity (mmol CO_2/g MMO)**			**Total CO_2 capacity (mmol CO_2/g ads)**		
	MgAl-MMO Powder	MgAl-MMO/rGO Aerogel	Capacity increase	MgAl-MMO Powder	MgAl-MMO/rGO Aerogel	Capacity increase
0.2 bar	0.28	0.71	154 %	0.28	0.55	96 %
1.0 bar	0.43	0.82	49 %	0.43	0.64	49 %
8.0 bar	0.91	3.02	236 %	0.91	2.36	159 %

It is worth mentioning that the MgAl-MMO/rGO aerogel also perform better than equivalent hybrid powders, such as MMO/rGO powders and MMO/CNT powders. Such carbon-supported powder sorbents have been investigated for elevated CO_2 sorption application in the literature, albeit only at low or atmospheric CO_2 pressures (p_{CO2}= 0.05-1 bar).[34, 47] When compared under these lower-pressure conditions, the MgAl-MMO/rGO aerogels show markedly higher intrinsic CO_2 adsorption capacity than equivalent MgAl-MMO/nanocarbon powders (see ESI Table S9), confirming the benefits of the robust, 3D-structured nanocarbon aerogel supports

over loose nanocarbon powder supports in terms of improved nanoparticle stabilisation and larger, more stable porosity.

In addition to their excellent CO_2 adsorption capacity, the MgAl-MMO/rGO aerogels also exhibit outstanding thermal regeneration stability for CO_2 sorption applications, similar to their organosulfur regeneration performance. After five regeneration cycles (see the experimental details in section 4), the CO_2 uptake of the MMO/rGO aerogel remains practically constant, retaining more than 90 % of its original capacity (at low, intermediate and high CO_2 pressures, Figure 7c). The stability obtained for the MgAl-MMO/rGO aerogel was found to be significantly higher compared to that of MMO adsorbents supported on rGO powder support, that retain less than 60 % of initial uptake under the same multicycle conditions.[47a, 47c] At high-CO_2-pressure conditions, previous studies of unsupported MMO sorbents have reported mechanical stability issues.[47c] In contrast, the MgAl-MMO/rGO aerogel exhibits excellent regeneration stability at high CO_2 pressures of up to 8 bar (Figure 7c).

The combination of high capacity and excellent regeneration stability makes the MgAl-MMO/rGO aerogels very promising candidates for pre-combustion CO_2 capture conditions. To the best of our knowledge, this work provides the first study characterising carbon-supported MMO sorbents at both high-CO_2-pressures *and* elevated temperatures (p_{CO2}= 8 bar, T= 300 °C). This work therefore provides valuable first materials systems and performance data for future studies (structure-function relationships, predictive modelling etc.) on the utilisation of supported MMOs for technologically-important high-pressure, elevated-temperature CO_2 sorption. Moreover, the electrical conductivity of the rGO aerogel support opens up new routes towards energy-efficient and uniform temperature control of the MMO-based CO_2 sorbents, with great future potential for rapid switching between CO_2 capture (thermally-activated CO_2 sorption) and sorbent regeneration (thermally-induced CO_2 desorption) via framework-mediated electrical heating (see also Figure 6). Although such electrical swing adsorption for

549 solid-state CO_2 sorbents is not yet established on the industrial scale, our findings provide
550 crucial insights for the future development of re-usable solid-state CO_2 sorbents, fundamentally
551 recyclable at low energy costs – important especially for the development of energy-efficient
552 SER processes.

553 **3. Conclusions**

554 This study introduces a facile route to uniformly support functional, LDH-derived
555 nanoparticles within nanocarbon aerogels at high weight loading in order to boost their
556 functional performance in both gas-phase and liquid-phase sorption applications. Specifically,
557 polymer-assisted assembly of LDH-decorated GO sheets was successfully adopted to support
558 metal oxide and metal nanoparticles (MgAl-MMO, NiAl-MNP, CuAl-MNP) within the
559 electrically-conducting framework of porous rGO aerogel supports at loading fractions of up
560 to 88 wt%. Supporting the LDH-derived nanoparticles within open, macroporous aerogels
561 results in outstanding improvements in their organosulfur adsorption characteristics, including
562 markedly increased organosulfur uptake capacities (both for simple and sterically-hindered
563 aromatic organosulfurs), 30 times accelerated adsorption kinetics, excellent organosulfur
564 selectivity and significantly improved sorbent regeneration stability. This work also provides
565 the first data for the sorption of CO_2 onto supported MMO nanoparticles at high-pressure,
566 elevated-temperature conditions (p_{CO2}=8 bar, T=300 °C), relevant to pre-combustion carbon
567 capture technologies. Under these conditions, the MgAl-MMO/rGO aerogel sorbents exhibit
568 excellent total CO_2 sorption capacities of up to 2.36 mmol CO_2/g ads (equivalent to 3.02 mmol
569 CO_2/g MMO). This uptake value constitutes a 160 % increase in total CO_2 capacity (compared
570 to the unsupported MgAl-MMO), and is higher than that reported for other solid-state sorbents
571 previously tested under comparable conditions. The excellent performance of the aerogel-
572 supported MgAl-MMO in two independent sorption applications clearly evidences the
573 excellent stabilising support function of rGO aerogels. Nanoparticle sintering and deactivation

574 during sorbent use and sorbent regeneration is efficiently inhibited due to strong anchoring of
575 the LDH-derived nanoparticles within the GO aerogel framework, while nanoparticle
576 accessibility is markedly improved due to the large and robust porosity of the aerogel support.
577 Future studies are likely to explore structure-function relationships in more detail (e.g.
578 investing impact of nanocarbon type, nanoparticle loading fraction, crosslinking density).

579 Further, our study demonstrates additional functionality enabled by the electrical conductivity
580 of the rGO aerogel support, specifically direct electrical framework heating of the supported
581 sorbent nanoparticles for thermal regeneration purposes. Sorbent regeneration via Joule heating
582 allows for regeneration of exhausted organosulfur sorbents at considerably lower energy cost
583 (>350 times less energy consumption than furnace heating) and shorter time scales (heating
584 rates of > 720 $K \cdot min^{-1}$) compared to conventional regeneration via external heating. In the
585 future, such electrical framework heating could be explored for applications beyond thermal
586 regeneration, for example for energy efficient temperature control in SER technologies or other
587 temperature-sensitive reaction processes. The macroscopic and monolithic form of the aerogels
588 and their well-controlled micro- and nano-scale porosity also provides new opportunities to
589 exploit aerogel-induced performance enhancement and energy-efficient electrical heating in
590 continuous flow processes to further push process efficiency and compatibility with existing
591 technological infrastructure. More generally, these findings will help to further unlock the
592 potential of nanoparticle/nanocarbon aerogel hybrids in a wide range of applications, including
593 pre-combustion CO_2 capture, heterogeneous catalysis, electro-catalysis and sensing.

594 **4. Experimental Section**

595 *Materials:* Graphene oxide (GO) was purchased from William Blythe Limited.
596 $Mg(NO_3)_2 \cdot 6H_2O$ (99%), $Al(NO_3)_3 \cdot 9H_2O$ (98%), $Ni(NO_3)_2 \cdot 6H_2O$ (99%) $Cu(NO_3)_2 \cdot 3H_2O$
597 (99%), sucrose, polyvinyl alcohol (PVA), dibenzothiophene (DBT),

598 dimethyldibenzothiophene (DMDBT), and biphenyl (BP) were purchased from Sigma-Aldrich.
599 NaOH, Na_2CO_3 and n-octane were purchased from Fisher Scientific UK, respectively. All
600 chemicals were used without further purification.

601 *Synthesis of LDH decorated GO aerogels:* Typically, 75 mg GO and 75 mg organic additives
602 (PVA and sucrose in a 1:1 weight ratio) were sonicated in 10 mL HPLC water to produce a
603 well-dispersed GO suspension. To this GO dispersion, a pre-fabricated wet-paste of MgAl-
604 LDH (containing about 210 mg MgAl-LDH, see below) was added, followed by dilution with
605 HPLC water to a total suspension volume of 10 mL. Then, 3.5 mL of the obtained suspension
606 was cast into bespoke cylindrical moulds for unidirectional freezing in liquid nitrogen for 10
607 minutes. Finally, the MgAl-LDH/GO aerogel was obtained by freeze-drying overnight using a
608 freeze-dryer (LABCONCO). The as-prepared aerogel was thermally reduced at 1000 °C, for 2
609 h, under N_2/H_2 atmosphere (5% H_2), using a tube furnace (Carbolite Gero Limited) to obtain a
610 MgAl-Mixed-Metal-Oxide/GO aerogel (MgAl-MMO/rGO aerogel) with an inorganic
611 adsorbent loading of around 78%. MgAl-MMO/rGO aerogels within different loadings were
612 also fabricated for specific Joule heating studies. Typical dimensions of the cylindrical hybrid
613 aerogel monoliths were 1.5 cm ×1.3 cm (cylinder diameter × cylinder height).

614 *Synthesis of LDH wet paste:* MgAl-LDH (Mg:Al=2:1) were produced through co-precipitation
615 of high concentration mixed metal salt solutions under alkaline conditions. The 2:1 cation ratio
616 was selected as an well-established stoichiometry with robust, repeatable materials
617 characteristics and performance metrics, allowing for reliable comparison of this study's
618 findings against literature results on pure MgAl-MMO powders with the same cation ratio.[28,
619 34] For the synthesis of MgAl-LDH wet-paste (Mg:Al ratio 2:1), a liquid solution (4.5 mL)
620 containing 0.5 M $Mg(NO_3)_2{\cdot}6H_2O$ and 0.25 M $Al(NO_3)_3{\cdot}9H_2O$ was added dropwise (2 min)
621 into an alkaline solution (5 mL) of 4.7 M NaOH and 1.2 M Na_2CO_3. The as-prepared white
622 suspension was aged under vigorous stirring at 60 °C for 16 h. The obtained white precipitate

was washed with HPLC water to neutrality. The washed LDH particles were recovered as wet paste (i.e. avoiding drying out at any stage of the washing or recovery process) and used immediately in the aerogel synthesis in order to minimise irreversible particle aggregation. Using MgAl-LDH paste produced under the above conditions directly in the aerogel synthesis resulted in an LDH loading of 78 wt% in the final hybrid aerogel; other loading fractions were achieved by reducing the volumes of the initial metal salt and alkaline solutions. NiAl-LDH (Ni:Al = 3:1) and CuAl-LDH (Cu:Al = 2:1) were synthesised through co-precipitation of the corresponding mixed metal nitrate solutions at constant alkaline pH (pH 10.5 and pH 10, respectively) and also recovered as wet-pastes (for synthetic details see ESI).

Organosulfur sorption: The adsorbent (60 mg) was added to a DBT solution in n-octane (initial DBT concentration 500 ppm) and stirred at 20 °C for 120 h (n-octane is a major component of gasoline with high organosulfur solubility and therefore frequently used as model fuel). Aerogel adsorbents were placed onto a bespoke porous sample holder within the DBT solution in order to avoid damage to the aerogel monolith through the stirrer bar (ESI Figure S19). Each sample was accompanied by a pure DBT reference solution in order to account for potential non-adsorbent-related variations in DBT concentration. To determine DBT equilibrium uptake values, aliquots of DBT solution were sampled after 120 h, centrifuged to sediment potential particle impurities, and then measured via gas chromatography (GC, Agilent 7890B GC system with an HP-5 column). The reduction in organosulfur GC peak area relative to the pure DBT reference was then used to calculate the quantity of adsorbed DBT. The intrinsic DBT uptake values of the adsorbents (in "mg·S/g MMO" units) are obtained from the ratio of adsorbed DBT quantity (in "mg·S" units) and the mass of MMO in the adsorbent (as determined by TGA). For the DMDBT experiments, an initial concentration of 500 ppm DMDBT in n-octane was used. For the measurement of sorption kinetics, aliquots were sampled at defined time intervals (2 h, 6 h, 12 h, 24 h, 72 h, 120 h). The corresponding DBT take values (in "mg·S/g

MMO" units) were plotted against time and fitted according to the pseudo-second-order model to obtain the DBT sorption rate constant (in "$g \cdot mg^{-1} \cdot h^{-1}$", where "g" relates to gram MMO in the adsorbent and "mg" relates to milligram sulfur in the adsorbate). For the testing of adsorbent selectivity, mixed BP and DBT solutions in n-octane (500 ppm BP and 500 ppm DBT) were used. The selectivity was quantified as ratio of molar DBT uptake relative to combined molar uptake of DBT and BP. For the regeneration experiments described in section 2.3, sorbents were removed from DBT solution (500 ppm DBT) after 120 h, thermally regenerated in a Muffle furnace at 250 °C, and then re-used in a fresh DBT solution (500 ppm DBT). The capacity retention values were determined by taking the ratio of the DBT uptake value after 3 regeneration cycles relative to the initial DBT uptake value of the as-synthesised sorbent. All experiments were carried out multiple times and exhibited high reproducibility.

Joule heating of hybrid aerogels: Joule-heating characterisation of the MgAl-MMO/rGO aerogel and thermal aerogel regeneration post organosulfur adsorption were conducted using a customized setup for direct electrical heating (Joule heating) of electrically-conducting monolithic materials under inert (N_2) atmosphere (ESI Figure S20). For the Joule-heating regeneration experiments, the MMO/rGO aerogel monolith was recovered from DBT solution after 120 h, mildly dried at room temperature and then placed within the Joule heating setup. The electrical current through the aerogel was then slowly increased until the aerogel surface temperature reached 250 ^{o}C (measured by K grounded tip insulated probe with thermocouple data logger, RS Components Ltd) and kept at this temperature for 1 h. After Joule heating regeneration, the intact aerogel was immersed into fresh DBT solution and the Joule heating procedure was repeated for three regeneration cycles. As comparison, thermal regeneration of pure MMO powders and MMO/rGO aerogels after DBT adsorption was also carried out in a Muffle furnace (250 °C, 5 ^{o}C/min ramping rate, see also ESI Table S7).

High-pressure, high-temperature CO_2 sorption: An Intelligent Gravimetric Analyser (Hiden Isochema, IGA 002, software HIsorp 2016) operating up to 20 bar was used to obtain adsorption isotherms under dry conditions. The samples (~10-50 mg) were pre-conditioned in situ under vacuum at 400 °C for 3 h using a standard furnace (operating up to 500 °C). The temperature was then decreased from 400 to 300 °C at 5 $K \cdot min^{-1}$ and held for 1 h. Adsorption isotherms were performed by switching the feed gas to pure CO_2. First contact adsorption isotherms at 300 °C were obtained by increasing CO_2 pressure from ~0.01 bar to ~10 bar using different pressure step sizes (step sizes between 0.5 bar to 5 bar), with a minimum step duration of 60 min. The stability of the adsorbents was measured by multicycle tests in which after the adsorption step, a desorption isotherm was carried out from ~10 bar to ~200 mbar keeping the temperature at 300 °C. Then the sample was degassed under vacuum at 400 °C for 1h. This procedure was repeated for 5 consecutive cycles. The multicycle experiments conducted are a combination of pressure and temperature swing regeneration. The data of each adsorption step are reported in this work. The adsorption capacity of the materials was determined from the change in mass during the adsorption steps.

Materials characterisation: Powder X-ray diffraction (XRD) was conducted on a Bruker D2 Phaser Diffractometer using CuKα radiation (λ = 1.54 Å) at 30 kV, 10mA, hold time of 2 s, and a step size of $\theta = 0.01013^{o}$. Crystallite domain sizes, D_p, were calculated using the Scherrer equation, while Braggs law was used to calculate lattice spacings, d. Scanning electron microscopy (SEM) was carried out using a Nova NanoSEM 450 with an accelerating voltage of 3 kV. Samples were fixed onto alumina stubs using conducting carbon tape and coated with a 2 nm Ir conductive layer before analysis. Energy dispersive X-ray spectroscopy (EDX) mapping was carried out on the same SEM instrument at an accelerating voltage of 18 kV without coating. Transmission electron microscopy (TEM) images were taken on an electron microscope (Tecnai F30, FEI) at an accelerating voltage of 300 kV. Samples were sonicated in

ethanol, followed by drop-casting onto a copper grid. Raman spectroscopy was performed using a Renishaw InVia with an excitation laser wavelength of 532 nm between 400 and 4000 cm^{-1}. Brunauer-Emmett-Teller (BET) surface area measurements were conducted using a Micromeritics TriStar 3000 instrument. The samples were degassed under N_2 gas at 110 ^oC for 3 hours prior to analysis, and N_2 adsorption and desorption isotherms were measured at 77 K. The pore diameter distribution of the samples was calculated from the desorption isotherm using the Barrett-Joyner-Halenda (BJH) method. Thermogravimetric analysis (TGA) in air was conducted on a TGA Q600 model (TA instruments) using a 5 ^oC/min ramping rate from 20 to 850 ^oC. The zeta potential values were measured, using a Malvern Zetasizer-Nano ZS model (Malvern Instruments Ltd.). The different pH values were generated through titration of 0.1 M HCl and 0.1 M NaOH, respectively. Aerogel compressibility measurements were performed on a Bose ELF 3200 machine. X-ray photoelectron spectroscopy (XPS) was carried out using a Thermo Fisher Scientific K-Alpha+; high-resolution scans were collected at a pass energy of 30 eV and a step size of 0.1 eV. The binding energies were referenced to the C 1s peak of adventitious carbon at 284.8 eV.

Supporting Information

Supporting Information is available from the Wiley Online Library or from the author.

Acknowledgements

This research was sponsored by the China Scholarship Council and the University of Leeds. We would like to thank Dr. Mary Bayana and Alex Schleif for their help.

References

[1] a) N. Yousefi, X. Lu, M. Elimelech, N. Tufenkji, *Nat. Nanotechnol.* **2019**, *14*, 107; b) R. Liu, Y. Xu, B. Chen, *Environ. Sci. Technol.* **2018**, *52*, 7043.

[2] S. Barg, F.M. Perez, N. Ni, P. do Vale Pereira, R.C. Maher, E. Garcia-Tunon, S. Eslava, S. Agnoli, C. Mattevi, E. Saiz, *Nat. Commun*. **2014**, *5*, 4328.

[3] K.Q. Lu, X. Xin, N. Zhang, Z.R. Tang, Y.J. Xu, *J. Mater. Chem. A* **2018**, *6*, 4590.

[4] C. Zhu, T.Y.J. Han, E.B. Duoss, A.M. Golobic, J.D. Kuntz, C.M. Spadaccini, M.A. Worsley, *Nat. Commun.* **2015**, *6*, 6962.

[5] M. Peng, Z. Wen, L. Xie, J. Cheng, Z. Jia, D. Shi, H. Zeng, B. Zhao, Z. Liang, T. Li, *Adv. Mater.* **2019**, *35*, 1902930.

[6] B. Chen, Q. Ma, C. Tan, T.T. Lim, L. Huang, H. Zhang, *Small* **2015**, *11*, 3319.

[7] J. Li, X. Yun, Z. Hu, L. Xi, N. Li, H. Tang, P. Lu, Y. Zhu, *J. Mater. Chem. A* **2019**, *7*, 26311.

[8] C. Cheng, S. Li, A. Thomas, N. A. Kotov, R. Haag, *Chem. Rev.* **2017**, *117*, 1826.

[9] W. Xia, C. Qu, Z. Liang, B. Zhao, S. Dai, B. Qiu, Y. Jiao, Q. Zhang, X. Huang, W. Guo, *Nano Lett.* **2017**, *17*, 2788.

[10] H. Zhuo, Y. Hu, X. Tong, Z. Chen, L. Zhong, H. Lai, L. Liu, S. Jing, Q. Liu, C. Liu, *Adv. Mater.* **2018**, *30*, 1706705.

[11] J.Y. Hong, B.M. Bak, J.J. Wie, J. Kong, H.S. Park, *Adv. Funct. Mater.* **2015**, *25*, 1053.

[12] B. Xia, Y. Yan, X. Wang, X.W.D. Lou, *Mater. Horiz.* **2014**, *1*, 379.

[13] M. Yan, Q. Jiang, T. Zhang, J. Wang, L. Yang, Z. Lu, H. He, Y. Fu, X. Wang, H. Huang, *J. Mater. Chem. A* **2018**, *6*, 18165.

[14] C. Tang, H.S. Wang, H.F. Wang, Q. Zhang, G.L. Tian, J.Q. Nie, F. Wei, *Adv. Mater.* **2015**, *27*, 4516.

[15] a) X. Xu, Y. Sun, W. Qiao, X. Zhang, X. Chen, X. Song, L. Wu, W. Zhong, Y. Du, *Appl. Surf. Sci.* **2017**, *396*, 1520; b) F. An, X. Li, P. Min, H. Li, Z. Dai, Z.Z. Yu, *Carbon* **2018**, *126*, 119.

[16] a) C. Teng, J. Qiao, J. Wang, L. Jiang, Y. Zhu, *Acs Nano* **2015**, *10*, 413; b) L. Xiao, D. Wu, S. Han, Y. Huang, S. Li, M. He, F. Zhang, X. Feng, *Acs Appl. Mater. Inter.* **2013**, *5*, 3764.

[17] J. Xiao, Y. Tan, Y. Song, Q. Zheng, *J. Mater. Chem. A* **2018**, *6*, 9074.

[18] M. Wang, X. Duan, Y. Xu, X. Duan, *Acs Nano* **2016**, *10*, 7231.

[19] a) L. Xu, G. Xiao, C. Chen, R. Li, Y. Mai, G. Sun, D. Yan, *J. Mater. Chem. A* **2015**, *3*, 7498; b) R. Menzel, S. Barg, M. Miranda, D.B. Anthony, S.M. Bawaked, M. Mokhtar, S.A. Al-Thabaiti, S.N. Basahel, E. Saiz, M.S. Shaffer, *Adv. Funct. Mater.* **2015**, *25*, 28.

[20] Z. Juanjuan, L. Ruiyi, L. Zaijun, L. Junkang, G. Zhiguo, W. Guangli, *Nanoscale* **2014**, *6*, 5458.

[21] B. Xie, Y. Zhang, R. Zhang, *J. Mater. Chem. A* **2017**, *5*, 17544.

[22] X. Xu, H. Li, Q. Zhang, H. Hu, Z. Zhao, J. Li, J. Li, Y. Qiao, Y. Gogotsi, *Acs Nano* **2015**, *9*, 3969.

[23] Y. Ma, Y. Yue, H. Zhang, F. Cheng, W. Zhao, J. Rao, S. Luo, J. Wang, X. Jiang, Z. Liu, *Acs Nano* **2018**, *12*, 3209.

[24] H. Huang, S. Yang, R. Vajtai, X. Wang, P. M. Ajayan, *Adv. Mater.* **2014**, *26*, 5160.

[25] Y. Hou, Z. Wen, S. Cui, X. Feng, J. Chen, *Nano Lett.* **2016**, *16*, 2268.

[26] Y. Song, H. Li, L. Yang, D. Bai, F. Zhang, S. Xu, *Acs Appl. Mater. Inter.* **2017**, *9*, 42742.

[27] Q. Fang, B. Chen, *J. Mater. Chem. A* **2014**, *2*, 8941.

[28] R. Menzel, D. Iruretagoyena, Y. Wang, S.M. Bawaked, M. Mokhtar, S.A. Al-Thabaiti, S.N. Basahel, M.S. Shaffer, *Fuel* **2016**, *181*, 531.

[29] a) S.A. Ganiyu, K. Alhooshani, K.O. Sulaiman, M. Qamaruddin, I.A. Bakare, A. Tanimu, T.A. Saleh, *Chem. Eng. J.* **2016**, *303*, 489; b) Y. Han, M.A. Sinnwell, S.J. Teat, M.L. Sushko, M.E. Bowden, Q.R.S. Miller, H.T. Schaef, L. Liu, Z. Nie, J. Liu, *Adv. Sci.* **2019**, *6*, 1802056; c) K.X. Lee, J.A. Valla, *React. Chem. Eng.* **2019**, *4*, 1357.
[30] T.A. Saleh, Nanotechnology in oil and gas industries: principles and applications, *Springer*, **2017**.
[31] J. Dong, T. Zhu, H. Li, H. Sun, Y. Wang, L. Niu, X. Wen, G. Bai, *Ind. Eng. Chem. Res.* **2019**, *58*, 14688.
[32] S. Choi, J.H. Drese, C.W. Jones, *ChemSusChem.* **2009**, *2*, 796.
[33] a) M. De Marco, R. Menzel, S.M. Bawaked, M. Mokhtar, A.Y. Obaid, S.N. Basahel, M.S. Shaffer, *Carbon* **2017**, *123*, 616; b) S. Radha, A. Navrotsky, *J. Phys. Chem. C* **2014**, *118*, 29836.
[34] A. Garcia-Gallastegui, D. Iruretagoyena, V. Gouvea, M. Mokhtar, A.M. Asiri, S.N. Basahel, S.A. Al-Thabaiti, A.O. Alyoubi, D. Chadwick, M.S. Shaffer, *Chem. Mater.* **2012**, *24*, 4531.
[35] D. Xia, H. Li, P. Huang, J. Mannering, U. Zafar, D. Baker, R. Menzel, *J. Mater. Chem. A* **2019**, *7*, 24027.
[36] a) S.I. Garcés-Polo, J. Villarroel-Rocha, K. Sapag, S. Korili, A. Gil, *Chem. Eng. J.* **2018**, *332*, 24; b) Z. Yong, V. Mata, A.E. Rodrigues, *Ind. Eng. Chem. Res.* **2001**, *40*, 204; c) M.J. Ramírez-Moreno, I.C. Romero-Ibarra, M. Hernández-Pérez, H. Pfeiffer, *Ind. Eng. Chem. Res.* **2014**, *53*, 8087; d) J. Boon, P. Cobden, H. Van Dijk, C. Hoogland, E.V. van Selow, M. van Sint Annaland, *Chem. Eng. J.* **2014**, *248*, 406.
[37] Y. Zou, X. Wang, Y. Ai, Y. Liu, J. Li, Y. Ji, X. Wang, *Environ. Sci. Technol.* **2016**, *50*, 3658.
[38] H. Zhu, X. Yang, E. D. Cranston, S. Zhu, *Adv. Mater.* **2016**, *28*, 7652.
[39] N. Carreño, M. Escote, A. Valentini, L. McCafferty, V. Stolojan, M. Beliatis, C. Mills, R. Rhodes, C. Smith, S. Silva, *Nanoscale* **2015**, *7*, 17441.
[40] Y. Gao, Z. Zhang, J. Wu, X. Yi, A. Zheng, A. Umar, D. O'Hare, Q. Wang, *J. Mater. Chem. A* **2013**, *1*, 12782.
[41] a) J. Kuljiraseth, A. Wangriya, J. Malones, W. Klysubun, S. Jitkarnka, *Appl. Catal. B Environ.* **2019**, *243*, 415; b) Y. Cheng, J. Lin, T. Wu, H. Wang, S. Xie, Y. Pei, S. Yan, M. Qiao, B. Zong, *Appl. Catal. B Environ.* **2017**, *204*, 475.
[42] W. Liu, J. Cai, Z. Ding, Z. Li, *Appl. Catal. B Environ.* **2015**, *174*, 421.
[43] a) R. Beams, L. G. Cançado, L. Novotny, *J. Phys. Condens. Mat*. **2015**, *27*, 083002; b) J.S. Li, Y. Wang, C.H. Liu, S.L. Li, Y.G. Wang, L.Z. Dong, Z.H. Dai, Y.F. Li, Y.Q. Lan, *Nat. Commun.* **2016**, *7*, 1; c) J. Mu, C. Hou, G. Wang, X. Wang, Q. Zhang, Y. Li, H. Wang, M. Zhu, *Adv. Mater.* **2016**, *28*, 9491.
[44] S. Guo, Y. Jiang, L. Li, X. Huang, Z. Zhuang, Y. Yu, *J. Mater. Chem. A* **2018**, *6*, 4167.
[45] J.J. Bae, S.C. Lim, G.H. Han, Y.W. Jo, D.L. Doung, E.S. Kim, S.J. Chae, T.Q. Huy, N. Van Luan, Y.H. Lee, *Adv. Funct. Mater.* **2012**, *22*, 4819.
[46] S. Pei, Q. Wei, K. Huang, H.M. Cheng, W. Ren, *Nat. Commun.* **2018**, *9*, 145.
[47] a) A. Garcia-Gallastegui, D. Iruretagoyena, M. Mokhtar, A.M. Asiri, S.N. Basahel, S.A. Al-Thabaiti, A.O. Alyoubi, D. Chadwick, M.S. Shaffer, J. Mater. Chem. **2012**, *22*, 13932; b) N.N. Meis, J.H. Bitter, K.P. de Jong, *Ind. Eng. Chem. Res.* **2010**, *49*, 1229; c) D. Iruretagoyena, M.S. Shaffer, D. Chadwick, *Adsorption* **2014**, *20*, 321.